Multi-rate unscented Kalman filtering for pose and curvature estimation in 3D ultrasound-guided needle steering

Guillaume Lapouge, Jocelyne Troccaz, Philippe Poignet

Multi-rate unscented Kalman filtering for pose and curvature estimation in 3D ultrasound-guided needle steering

G. Lapouge[a,b,*], J. Troccaz[a], P. Poignet[b]

[a] *Univ. Grenoble Alpes, CNRS, Grenoble INP, TIMC-IMAG, F-38000 Grenoble, France*
[b] *Univ. Montpellier, CNRS, LIRMM, F-34090 Montpellier, France*

Abstract

This paper presents a new method for estimating the needle pose and curvature in the context of robotically steered needles. The needle tip trajectory is represented by a modified unicycle kinematic model. A multi-rate unscented Kalman filter is proposed for the first time in needle steering to fuse asynchronous data coming from 3D B-mode ultrasound images, robot sensors and pre-operative elastography measurements. To demonstrate it, 51 unconstrained 3D insertions have been made in various media. The instantaneous localisation error is smaller than 0.6 mm and the prediction of the final tip position is smaller than 2 mm based on the observation of the first 2 cm of 8 cm deep insertions.

Keywords: Needle steering, Surgical robotics, Multi-rate unscented Kalman filter, 3D ultrasound imaging

1. Introduction to needle steering

In percutaneous operations, the needle is often inserted by the clinician under ultrasound (US) guidance. Because the clinical efficacy of such procedures is closely linked to the surgeon's ability to reach a specific target with a needle, robotically assisted needle guidance also referred to as "needle steering" has appeared and been the object of intensive research.

There are several ways to steer a needle in soft tissue. In this paper, the focus is put on bevel-tip needles which naturally bend when inserted in soft media. This phenomenon is due to the needle-tissue asymmetric interaction forces. This makes it possible for an expert practitioner to steer a needle to avoid an obstacle and to compensate for the tissue motion during the insertion. Such a deflection is however difficult to predict and to control manually, hence the need for surgical robotics.

One challenge in needle steering is to locate and estimate the current pose of the needle in images, for instance ultrasound volumes, and predict its future deflection. Solving this problem may rely on modelling the needle and developing an observer.

A first kinematic model is introduced in [23]. It shows that bevel-tip needles follow a circular path when inserted in homogeneous phantoms. This model has been successfully used by many studies ([1],[6] and [18]). However, in most studies, the radius of curvature has been considered constant during the insertion with few exceptions. This radius of curvature is often obtained by prior insertions. Such an approach is incompatible with a clinical application.

The curvature of the needle depends on the stiffness of the tissue it penetrates. It has been studied in [17] where the curvature estimation is done both online and offline: online by doing pure insertions and fitting a circle with the acquired planar trajectory; offline with pre-operative elastography measurements. In [6] a real-time needle shape prediction is proposed using a particle filter in the case of planar insertions. Unlike these studies, the solution detailed here is an estimator based on a fully 3D-compatible kinematic model. It takes into account the elasticity of the media and does not constrain the insertion to be planar.

*Corresponding author
Email addresses:
guillaume.lapouge@univ-grenoble-alpes.fr (G. Lapouge), jocelyne.troccaz@univ-grenoble-alpes.fr (J. Troccaz), philippe.poignet@lirmm.fr (P. Poignet)

Declarations of interest: none

Dynamic model-based deflection estimation has also been proposed for 2D [13] and 3D [8] steering. The approach looks promising and has been validated using 2D ultrasound feedback [21].

With the exception of [7] and [15], there is to our knowledge no recent work about needle steering based solely on 3D B-mode US images. The reason lies in the strong presence of artefacts and noise of such images.

Needles are hard to detect when they are thin or are not perpendicular to the US probe plane [11]. Many solutions ([1], [9], [17], and [20] among others) involve the use of a 2D probe that is translated to follow the needle tip. This solution to observe the needle also called 2.5D aims to keep the needle axis orthogonal to the imaging plane. In this way, the needle is always in the configuration of the maximum visibility and images are acquired at around 30Hz. Unfortunately, it is not practically feasible for most clinical operations. In addition, the movements of the probe may cause tissue deformation and may affect the needle deflection.

To avoid B-mode US imaging quality issues, Doppler mode imaging has also been exploited in [3] and in [14]. Although the needle visibility is improved by this imaging modality, specific needle movements are required and the overall precision of this imaging mode is lower than that of B-mode imaging.

As detailed above, there exists a broad variety of solutions for needle pose estimation and prediction, each of them validated on different experimental setups. Therefore, a direct quantitative comparison is made difficult.An overview of some of the most relevant observers in needle steering can be found in Appendix A.

A clinically-compatible 3D US probe with a 1 Hz refresh rate is used here in B-mode. The limited quality of the images and low frame rate are compensated by the precise estimation of the next needle tip pose. It specifies a region of interest for the next segmentation and decreases the likelihood of losing the needle tip in US volumes.

In this paper, an observer taking all available data as input to estimate the needle tip position and predict its future deflection is proposed. A multi-rate approach has been selected to fuse the needle rotation and insertion information provided by the robot, and measurements deduced form the pre-operative shear wave elastography imaging and intra-operative B-mode US volumes.

This paper is composed of two parts :

- In section 2, the advantages and limitations of the 3D ultrasound imaging are developed. The model chosen to describe the behaviour of the needle tip is detailed. The proposed observer is then presented.
- In section 3, the observer is first validated through simulation. Then, it is experimentally validated with 51 insertions made with various 24 gauge (0.51 mm diameter[1]) needles with asymmetric tips. These insertions are made in phantoms and pork tissue samples.

2. Methods

As already mentioned, 3D ultrasound imaging and kinematic modelling of the needle are considered here. Based on these choices, the methods employed in this paper are detailed below.

2.1. 3D Ultrasound Imaging

B-mode imaging

In this paper, a motorised end fire transrectal ultrasound probe represented in Figure 1 is set at a fixed position and works in B-mode imaging. 3D volumes are reconstructed from images acquired by rotating an array of piezoelectric transducers located in the probe head. The major drawback of such a setup is the limited image quality it provides. Indeed, when the needle is not orthogonal to the US emission direction, strong artefacts appear [11].

The lack of visibility of fine needles in 3D US volumes is due to their shape. The US waves reflect on the needle smooth surface in one direction and do not hit the transducer back. One possible refinement for regular B-mode imaging would involve roughening the surface of the needle so that the US waves diffuse in all directions and reflect back to the transducer.

Clinically compatible solutions to roughen the needle surface exist such as micro laser etching [16]. However, because of the high complexity of this process, a non-clinical approach applied here is to coat needles with polyurethane foam [11] (see Figure 2).

[1] Unit conversion table available at https://en.wikipedia.org/wiki/American_wire_gauge.

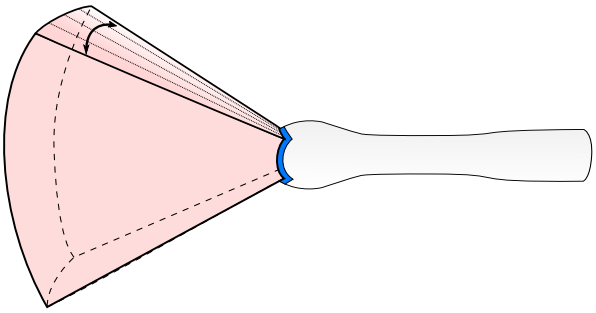

Figure 1: 3D volume (in red) acquired by a motorised end-fire transrectal ultrasound probe. The sweep direction of the transducer is indicated by an arrow.

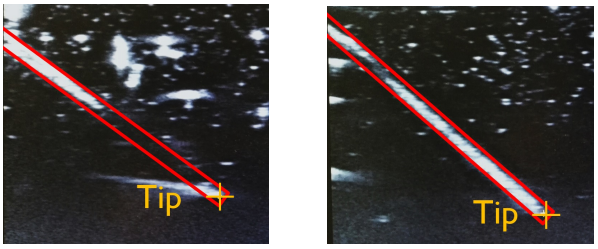

(a) Without surface treatment

(b) With polyurethane coating

Figure 2: 2D US acquisitions of needles inserted in soft tissue. The needle body is represented by a red frame and the needle tip by an orange cross. The use of polyurethane coating improves the needle visibility.

Because the needle visibility depends on the needle position and distance to the transducer and the medium it penetrates, the discernibility of the needle is predictable. The visibility quality can be taken into account by the estimator through the measurement noise covariance matrix.

Shear wave elastography imaging

The second imaging modality used in this paper is shear wave elastography imaging (see Figure 3). The propagation of an acoustic radiation force impulse is observed and used to compute Young's Modulus of a soft tissue characterising its elasticity properties [5]. The radius of curvature of the needle is correlated to the tissue elasticity properties. Therefore, shear wave elastography imaging (SWE) provides a rough measurement of the needle curvature.

2.2. Modified unicycle kinematic model

First introduced in [23], the bicycle kinematic model has since been validated and embraced by

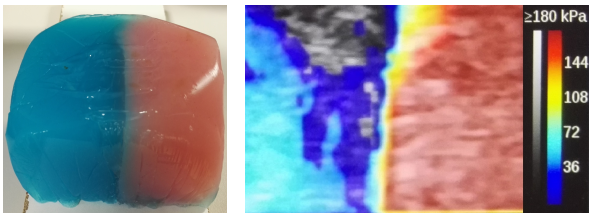

(a) Two-layer Agar phantom

(b) Corresponding shear wave elastography measurements

Figure 3: Shear wave elastography images of an Agar phantom with different elasticities. The red part is stiffer than the blue part.

most researchers in needle steering. A bevel-tip needle supposedly traces a circular path when inserted inside homogeneous tissues. The arc direction is related to the beveled tip orientation. However, when rotated at 180°, the needle follows another arc that is not tangent to the previous path. The so-called cutting angle is defined as the angle between the tangents to the trajectory before and after the rotation (see Figure 4).

The bicycle model is replaced in [2] by a modified unicycle model including the cutting angle. This model is easy to implement, while representing a similar needle tip behaviour. Therefore, it has been chosen in this paper.

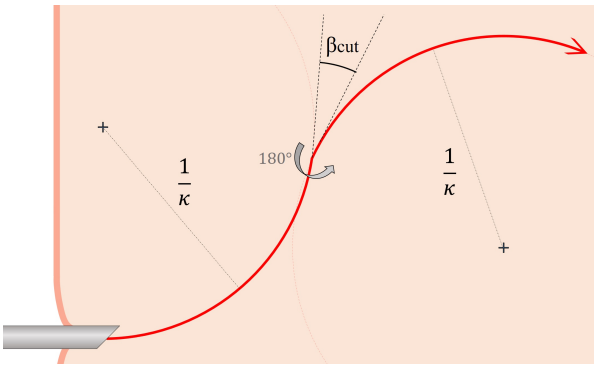

Figure 4: Needle tip behaviour following the modified unicycle kinematic model. Insertion with an instantaneous rotation of 180 °. Trajectory in red, β_{cut} is the cutting angle presented in 2.2, κ is the curvature of the needle path.

The joint state-space representation of this kinematic model can be written as $\dot{\mathbf{x}} = \mathbf{f}(\mathbf{x}, \mathbf{u})$ verifying

$$\begin{bmatrix} \dot{x} \\ y \\ z \\ \alpha \\ \beta \\ \gamma \\ \kappa \end{bmatrix} = \begin{bmatrix} \cos\alpha\cos\beta & 0 \\ \sin\beta & 0 \\ \cos\beta\sin\alpha & 0 \\ \kappa\cos\gamma\sec\beta + \kappa\frac{\beta_{cut}}{2}\sin\gamma\cos\gamma\tan\beta & -\frac{\beta_{cut}}{2}\sin\gamma \\ \kappa\sin\gamma - \kappa\frac{\beta_{cut}}{2}\cos\gamma\cos\gamma\tan\beta & \frac{\beta_{cut}}{2}\cos\gamma \\ -\kappa\cos\gamma tan\beta & 1 \\ 0 & 0 \end{bmatrix} \begin{bmatrix} u_1 \\ u_2 \end{bmatrix} \quad (1)$$

where x, y, z are the Cartesian coordinates of the needle tip in the 3D US volume frame [mm]; α, β and γ are the yaw,pitch and roll of the needle tip [rad]; κ is the curvature of the needle tip trajectory [mm^{-1}]. The inputs u_1 and u_2 correspond to the insertion speed [$mm.s^{-1}$] and the rotation speed [$rad.s^{-1}$] of the needle tip respectively. β_{cut} is the cutting angle presented in Figure 4. β_{cut} is deduced from data fitting done with several insertions. It varies from 0° to 6° and is proportional to the medium stiffness with low sensitivity and inversely proportional to the needle stiffness with high sensitivity. Because this calculation cannot be done in clinical procedures for each patient, β_{cut} is assumed to be purely needle-related.

2.3. Multi-rate unscented Kalman filter

Multi-rate filtering

The state-space representation described in (1) is incorporated in an unscented Kalman filter that runs at 100Hz. For the sake of brevity, detailed explanation of the functioning of unscented Kalman filters can be found in [22] and detailed equations can be found in Appendix B.

The available measurements come from sensors with different sampling rates: about 1 Hz for 3D US imaging and 100 Hz for robot position sensors. Therefore, the needle tip Cartesian position is acquired every second, and the angle of rotation of the needle around its axis every 10 ms. In the hypothesis that the term "$\kappa\cos\gamma\ tan\beta\ u_1$" in (1) remains small, the needle base rotation angle is a good estimate of the roll angle γ. Besides, pre-operative shear wave elastography (SWE) measurements can be considered asynchronously to obtain information on the radius of curvature of the needle. The asynchronous functioning is illustrated in Figure 5.

The measurement equation, when all measurements are available and the hypothesis are verified, can be written as

$$\mathbf{h}(\mathbf{x}) = \begin{bmatrix} x & y & z & \gamma & \kappa \end{bmatrix} \quad (2)$$

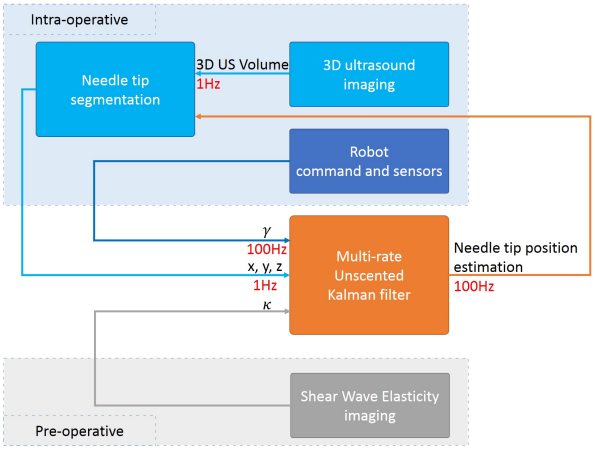

Figure 5: Proposed structure of the multi-rate unscented Kalman filter. Data flows are represented by arrows. Refresh rates are indicated in red when specifiable.

To fuse asynchronous data, a multi-rate approach of the unscented Kalman filter as presented in [4] is adapted here. The multi-rate unscented Kalman filter only takes the available measurements into consideration. Therefore, the matrices of the Kalman filter change size with respect to the measurements available at the current step time (indicated by an index Δ in Appendix B).

For example, among 8 possibilities, $\mathbf{h}_\Delta(\mathbf{x}) = \begin{bmatrix} x & y & z \end{bmatrix}$ if only the Cartesian position is measured , $\mathbf{h}_\Delta(\mathbf{x}) = [\gamma]$ if only the rotation is measured, and $\mathbf{h}_\Delta(\mathbf{x}) = \begin{bmatrix} x & y & z & \gamma \end{bmatrix}$ if both are measured. As for concerned matrices, the terms corresponding to unmeasured terms are removed.

Characterisation of measurement and process noise

Throughout the article, the segmented needle tip position is considered as a measure of the true needle tip position with zero mean gaussian noise. To characterize it, Cartesian coordinates provided by needle tip segmentation in 3D US volume have been found by doing 20 manual segmentations of the same tip pose located in the vicinity of the transducer. The resulting measurements showed a standard deviation (std) of 0.3 mm in each direction. The measurements - provided by the robot - of the needle base rotation have a std of 0.2 °. In addition, curvature measurement noise has been deduced from 51 insertions made in various phantoms with elasticity measured with SWE imaging. Assuming that the measurement noise is a white gaussian noise with zero mean, the covariance matrix of

the observation noise is taken equal to

$$\begin{aligned} &\mathbf{R} = diag(\sigma_x^2 \quad \sigma_y^2 \quad \sigma_z^2 \quad \sigma_\gamma^2 \quad \sigma_\kappa^2) \\ &with \\ &\sigma_x = \sigma_y = \sigma_z = 0.3\ mm \\ &\sigma_\gamma = 3.5.10^{-3}\ rad \\ &\sigma_\kappa = 1.10^{-3}\ mm^{-1} \end{aligned} \tag{3}$$

Based on the detailed study of the process noise made in [3], we have chosen the covariance matrix of the process noise as

$$\begin{aligned} &\mathbf{Q} = diag(q_x^2 \quad q_y^2 \quad q_z^2 \quad q_\alpha^2 \quad q_\beta^2 \quad q_\gamma^2 \quad q_\kappa^2) \\ &With \\ &q_x = q_y = q_z = 2.10^{-3}\ mm \\ &q_\alpha = q_\beta = 2.10^{-5}\ rad \\ &q_\gamma = 5.10^{-4}\ rad \\ &q_\kappa = 2.10^{-6}\ mm^{-1} \end{aligned} \tag{4}$$

The differences with [3] are introduced empirically to reflect the high frequency of the Kalman filter and the uncertain behaviour of very fine Nitinol needles. Again, the measurement noise is assumed to be white gaussian with a zero mean.

Matrix reset

When crossing the interface between two media with different elasticities, the radius of curvature of the needle path is expected to change. To detect such an interface, from the shear wave elasticity imaging, a map of tissue stiffness is acquired. Regions of similar elasticity can then be defined so as to divide the media into homogeneous partitions separated by these interfaces.

Because the error covariance matrix $\mathbf{P}$ defines how much the UKF trusts the current estimation, the diagonal term of $\mathbf{P}$ concerning κ is reset when crossing an interface. This expresses the expectation of a change in curvature and allows for a greater variation in the curvature estimation.

Considering minimal knowledge about the needle tip behaviour, $\mathbf{P}_0$, the initial value of $\mathbf{P}$ is defined as

$$\begin{aligned} &\mathbf{P}_0 = diag(p_x \quad p_y \quad p_z \quad p_\alpha \quad p_\beta \quad p_\gamma \quad p_\kappa) \\ &with \\ &p_x = p_y = p_z = 1mm \\ &p_\alpha = p_\beta = 5.10^{-3}\ rad \\ &p_\gamma = 1.10^{-1}\ rad \\ &p_\kappa = 2.10^{-6}\ mm^{-1} \end{aligned} \tag{5}$$

These values were chosen as the variance of an overestimated Gaussian initialisation noise (see Section 3.2 for more details on US volume-based initialisation).

The quality of the needle visualization in 3D US volumes strongly depends on its distance and orientation with respect to the ultrasound probe (see [19] for more details). Therefore, the terms corresponding to the Cartesian coordinates measurements of the matrix $\mathbf{R}$ are reset to take into account such a quality loss. Far from the transducer, the measurements are considered noisier and the corresponding terms are set at higher values.

Standard deviations of the Cartesian coordinates are reset such as $\sigma_c^{init} = (1 + a\frac{d}{d_{max}})\sigma_c$, where c stands for either x, y or z. σ_c^{init} are the reinitialised standard deviations of the Cartesian coordinates. σ_c are the ones found in the best measurement case and detailed in (3). d is the distance between the segmented needle tip and the transducer. d_{max} is the acquisition depth of the transducer (set to 8cm here). $a \in \mathbb{R}^+$ reflects the quality loss of the signal set thanks to prior segmentations (set to 1 here after experimental trials).

Constraints

In the model introduced in (1), the curvature κ is defined as a positive real number bounded by κ_{max}, the maximum curvature. To account for these restrictions, the estimated curvature is constrained with respect to

$$\kappa_t = \begin{cases} \kappa_t & \text{if } 0 \leq \kappa_t \leq \kappa_{max} \\ \kappa_{t-1} & else \end{cases}$$

κ_t being the current curvature estimation at time t and κ_{t-1} the previous estimation.

Although for all simulations and insertions, the curvature has always converged without any blow up. Such a constraint may not only limit the possible overshoot in curvature estimation, but also prevents the estimated curvature from becoming negative when the real curvature is close to zero.

3. Results

3.1. Simulation

State and measurements

The simulations help validate the robustness of the observer by comparing the estimation of the needle tip pose to the real tip pose. The simulation of the needle behaviour relies on the model described in (1) running at 100 Hz. The measurement vector of varying size is described in (2). A zero mean gaussian noise vector is added to the state and measurement vectors with the standard deviations described in (3) and (4).

Initialisation

To evaluate the effect of state initialisation on the error of the final tip position estimation, simulations with various initialisation error values on both the orientation of the tip and the curvature were run.

The error on the final tip Cartesian position depicted in Figure 6 shows a fast convergence of the estimator despite a high error in initialised orientation. It is compensated after 20 mm of observation.

On the other hand, a wrong initialisation of the radius of curvature induces a slow convergence of the final position estimation error.

An accurate initialisation of the radius of curvature is therefore crucial compared to orientation initialisation.

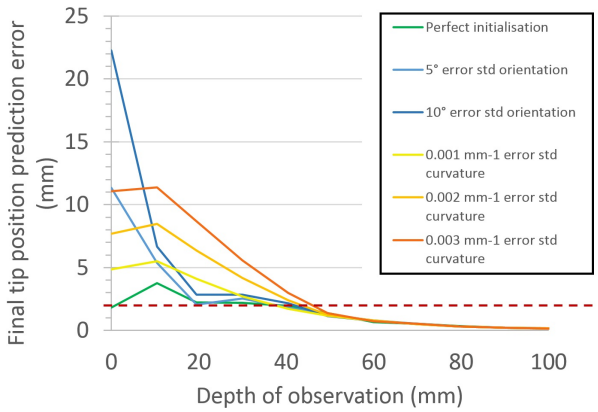

Figure 6: Evolution of the final position prediction error with the depth of observation. Zero mean gaussian noises on orientation and curvature initialization are applied and act on the filter convergence speed. The results are obtained over 100 simulated insertions.

Performance of the estimation

To characterise the performance of the proposed solution, 100 pure insertions at 1.5 mm.s^{-1} have been simulated.

The estimator values are initialised as the first measurement for all parameters when available. α and β are initialised with their real values added to a 5° std white gaussian noise.

The mean posture estimation errors reported in Table 1 show a good estimation of the needle tip trajectory. The average error is equal to 0.3 mm in position corresponding to the measurement noise and less than 1° in orientation.

	Mean	Std	Max
$E_{x,y,z}$ (mm)	0.3	0.1	1.3
E_α (°)	0.6	1.1	16.4
E_β (°)	0.9	1.1	11.5
E_κ (mm^{-1})	0.0007	0.0006	0.0136

Table 1: Instantaneous state estimation error deduced from 100 simulations. Mean, standard deviation and maximum error values are reported.

The final tip position estimation error depicted in Figure 6 decreases with the number of measurements and the depth of observation. It is sensitive to the initialisation of the filter, mostly to α, β, γ and κ. The threshold for good prediction is chosen to match the mean spatial resolution of the US probe used here, equal to 2 mm. The mean prediction error becomes satisfactory after 40 mm of insertion. This estimator is therefore robust to large initialisation error and provides sufficient estimation quality after observing 40% of the insertion length in the worst scenario possible. The estimation can then be used as feedback to steer the needle more precisely.

Effect of rotations on the estimation

One of the advantages of this observer is that it does not constrain the needle path to be composed of circular arcs or to be a single-plane motion. Nonetheless, if the needle rotates very fast around its axis, the apparent radius of curvature is null. No information about the curvature parameter κ can then be deduced from the insertion. This lack of information on the curvature also happens when the needle is rotated at 180 ° for similar reasons. The filter ability to estimate parameters remains linked to the control inputs. Such an effect can be quantified by simulating insertions with various needle rotation speeds u_2 and with orientation changes.

Figure 7b shows the temporal evolution of the diagonal term of $\mathbf{P}$ corresponding to the error covariance of κ. Faster rotations induce a slower convergence of this term, thus a slower estimation of the real curvature (cf. Figure 7a) which may decrease the precision of the estimation. Instantaneous rotations close to 180 ° also induce lag on the estimation. The convergence of the observer concerning the other state variables are not affected by the rotations in a significant way.

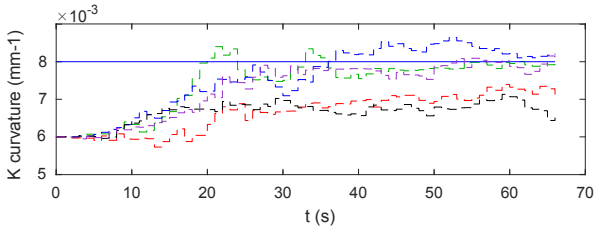

(a) Evolution of the curvature estimation (dotted lines) compared to the ground truth (line) as a function of time.

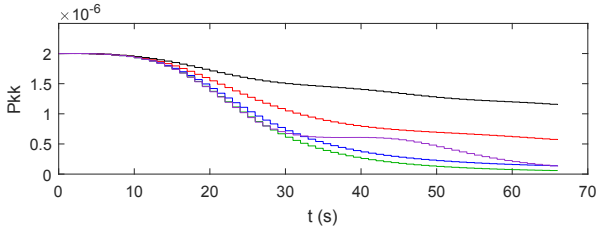

(b) Convergence of the estimation error covariance term corresponding to κ as a function of time.

Figure 7: Simulated curvature estimation for an insertion speed u_1 of 1.5 $mm.s^{-1}$. Variable rotation speeds u_2 are applied: no rotation (green); 180° orientation change at t = 25 s (purple); constant rotation speed u_2 of 0.09 $rad.s^{-1}$ (blue), 0.19 $rad.s^{-1}$ (red) and 0.28 $rad.s^{-1}$ (black).

Heterogeneous media

During a percutaneous procedure, the needle will go through tissues with various elasticities. The stiffer the medium is, the more efforts will be exerted at the needle tip and the higher the curvature will be. To account for these elasticity changes, the matrix reset is proposed in Section 2.3.

To simulate such a change in tissue elasticity, simulations in which the actual radius of curvature is a step function have been run. As plotted in Figure 8, the observer converges towards the new curvature with a speed and stability linked to the initialisation of the corresponding term in $\mathbf{P}$. The higher $P_{\kappa\kappa}$ is initialised, the faster the observer converges towards κ at the cost of precision.

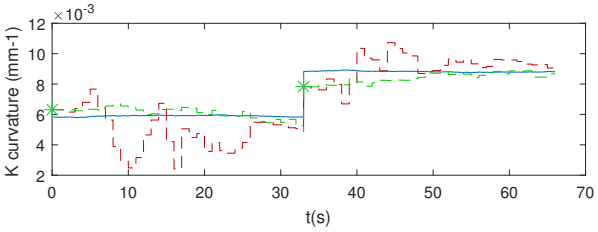

(a) Curvature estimation (dotted line) compared to the ground truth (line) and noisy measurements from elastography (asterisk).

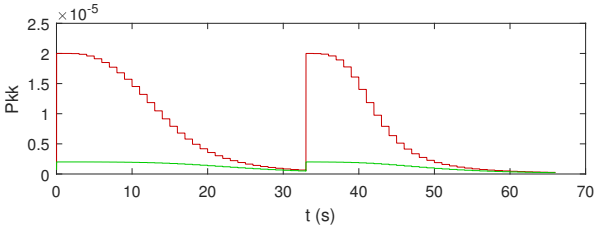

(b) Evolution of the covariance matrix term corresponding to κ as a function of time.

Figure 8: Simulation of curvature estimation in heterogeneous media. In green, classic reset of $P_{\kappa\kappa}$. In red, ten times greater reset of $P_{\kappa\kappa}$.

3.2. Experiments

Experimental setup and procedures

The system is composed of a robot holding the needle to insert it in a phantom. The insertion is observed with a 3D probe as depicted in Figure 9. The robot used for needle insertion has been developed by Hungr [12] for prostate brachytherapy. The ultrasound volumes are acquired every second with a 3D end-fire probe 4DEC-9/10 used with the Ultrasonix Sonix RP ultrasound system. The US volume voxels are cubes with 0.4 mm edges. The parameters defining the scaling of the unscented Kalman filter are classically chosen such that $\alpha_{UKF} = 0.001$, $\kappa_{UKF} = 0$, $\beta_{UKF} = 2$.

The proposed observer was implemented in the CamiTK framework [10]. It was coded in C++ with the help of the Eigen library known for its efficiency to cope with size varying matrices. Running on an Intel® Xeon® E3-1240 processor at 3.50 GHz, an iteration of the multi-rate Unscented Kalman filter takes 2.8 ± 0.5 ms. This is compatible with the 100 Hz refresh rate presented here.

A first set of phantoms has been made with paraffin gel mixed with a polymer additive called Vybar

to achieve different elasticities. These phantoms were used for 6 cm deep insertions. Deeper than this, the US waves were absorbed by the material. A second set of phantoms is made with Agar (Sigma A-7002) with varying concentrations (1% 2% and 5% of the water weight) for a variable stiffness. The good US propagation in such phantoms allowed for 9 cm needle insertions. Three different 24 gauge needles have been inserted at 1.5 mm.s^{-1} in several media and with various rotation schemes to validate the robustness of the estimator with 51 insertions. The rotation speed of the needle is chosen as either zero, piecewise constant, or peaks corresponding to a quick orientation changes of the needle around its axis.

For all insertions, the hypothesis concerning γ and formulated in Section 2.3 was verified as illustrated in Figure 11a. Indeed, let's set $\dot{\gamma_1} = \kappa \cos\gamma tan\beta u_1$ (cf. (1)) and $\dot{\gamma} = \dot{\gamma_1} + u_2$. Then, when a rotation speed is applied, $u_2 \gg \dot{\gamma_1}$ and $\dot{\gamma} \approx u_2$. Besides, when the rotation speed is null, the term $\dot{\gamma_1}$ is negligible when compared to possible needle torsion or other angles evolutions. It is therefore considered $\dot{\gamma} = u_2$ and γ is taken as equal to the needle base rotation angle.

The needle tip was segmented manually to define the real tip position. Because the ground truth is unknown, the Cartesian error is computed considering the segmented tip as the real needle tip position.

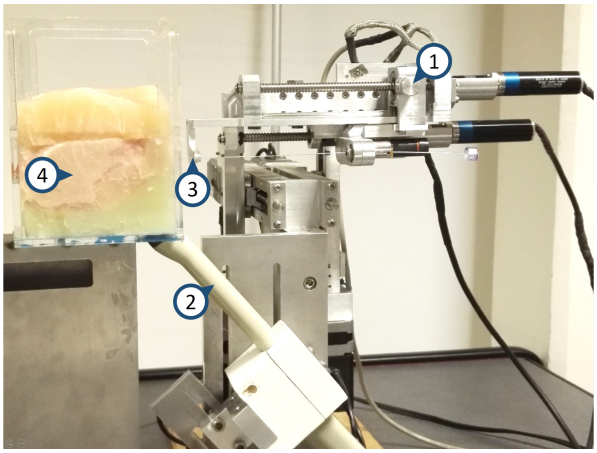

Figure 9: Experimental setup composed of the Prosper Robot (1), 3D US imaging system (2), Beveled-tip needle (3) and Pork tissue incorporated in Agar (4).

Initialisation

State initialisation is achieved by segmenting a visible small length of needle in a pre-insertion US volume. The segmentation result is an Euclidean vector pointing from the needle's visible base to its tip. From this vector, the initial Cartesian position of the needle, its yaw and pitch are deduced. The bevel-tip rotation is initialised as the robot corresponding sensor measurement. Curvature initialisation relies on elastography using the relation between tissue elasticity and curvature similarly to [17] and deduced from prior insertions in phantoms with known elasticity. The error and the observation noise covariance matrices follows the reset protocol described in Section 2.3.

Insertions in homogeneous phantoms

For preliminary experimental validation, 41 insertions have been made in homogeneous phantoms.

A first example of insertion is shown in Figure 10[2] while four insertions are detailed in Figure 11. Estimation error results can be found in Table 2 and Figure 12. Again, these results are not restricted to planar trajectories, they concern all kind of 3D insertions.

As seen in Table 2, the error varies with the medium and the needle material used.

	# of insertions	$E_{mean}(mm)$	$E_{std}(mm)$	$E_{max}(mm)$
Agar S-BT	12	0.5	0.3	1.9
Agar N-BT	13	0.6	0.3	2.6
Paraffin S-PC	16	0.6	0.4	6.0

Table 2: Instantaneous tip position estimation error. S-BT : Steel bevel-tip needle, N-BT : Nitinol bevel-tip needle, S-PC : Steel pre-curved needle.

Difference in performance among the different media and needles might be explained by their properties. First, the needle is more distinguishable in water-based media such as Agar that provide better US image quality than paraffin. Finally, insertions with higher curvature are likely to behave more randomly. The difference in performance with the simulations (cf. Table 1) may be explained by the difference in the calculation of the error itself. Indeed, the error here is deduced only from noisy measurements and not the unavailable ground truth. Using the same mean of calculation for simulated insertions entails similar error values.

[2]Detailed video of the insertion available at https://youtu.be/bVWG8aIJp5A. A slight difference can be observed between the estimated tip path and the final needle pose. This expected difference shows that the needle body does not exactly follow the needle tip.

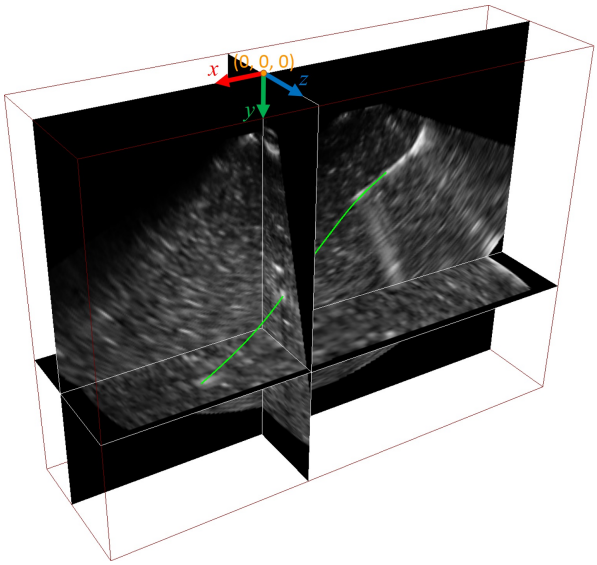

Figure 10: 3D US volume of a needle inserted in an Agar phantom. The volume is represented by three planar sections. Estimated needle tip path represented by the green curve (for detailed data, see green curve in Figure 11). Developed in the CamiTK framework [10].

These instantaneous localisation results represent an improvement on the 3D US based method developed in [15]. Besides, the results are on par with [8] and [17] in spite of the better image quality provided by the corresponding sensors (see Appendix A for more details).

The mean prediction error of the final tip position, plotted in Figure 12, is smaller than 2 mm after observing the two first centimetres of the insertion. The estimator performance is therefore satisfying for prediction starting from 25% of the total insertion length. In spite of more difficult conditions (thin needles, 3D steering, 3D US), these prediction results seem to be more satisfactory than those in [6] and [21]. However this comparison must be put into perspective, as the insertion length and experimental setup differ from these works (see Appendix A for more details).

Insertions in heterogeneous phantoms

Heterogeneous media may have variable stiffnesses which modify the radius of curvature of the needle path. A set of two-layer phantoms has been made using different concentrations of Agar (shown in Figure 3a). Using pre-operative measurements of the phantom elasticity, the matrix resetting described in Section 2.3 is applied: $\mathbf{P}$ is reset at the interface between two layers while $\mathbf{R}$ is reset continuously.

A curvature estimation done on a two-layer Agar phantom is plotted in Figure 13. The needle is inserted in the softer part of the Agar phantom. The needle tip then penetrates into the second layer after 34 mm of insertion. Performance wise, the matrix reset process induced a faster convergence of the curvature estimation. Using pre-operative elastography measurements, the final tip deflection estimation error decreases from 5.8 mm to 2.2 mm. Without knowledge of where the elasticity changes, the observer converges anyway but slowly. The instantaneous tip estimation remains similar while the prediction quality decreases.

Insertions in biological tissue

Phantoms and biological tissues have different mechanical properties. A first step towards clinical validation of the presented solution is to experiment on biological tissue. To do so, 10 insertions have been made in pork tenderloin and liver with 24 gauge beveled-tip nitinol needles. The overall performance of the estimator remains very close to the case of homogeneous-phantom insertions presented in Table 2. Indeed, the instantaneous error on the tip position estimation is equal to 0.69 ± 0.34 mm which is comparable to the paraffin results. The decrease in performance can be explained by the media properties: biological tissues contain fibres and heterogeneities that may induce a higher randomness of the needle behaviour.

As detailed above, the observer is compatible with biological tissue insertions. This is very promising for future clinical applications.

4. Concluding remarks

This paper presents an observer capable of estimating the needle pose and curvature, compatible with 3D needle steering and 3D US probes used in B-mode. As already mentioned, unlike in [17] or [20], the proposed solution does not constrain the needle movement. Besides, it is among the few existing works with [7] and [15] to work with 3D B-mode US imaging.

The observer fuses asynchronous information coming from the robot, the US imaging system and shear wave elastography measurements. The orientation, curvature and position of the needle tip are

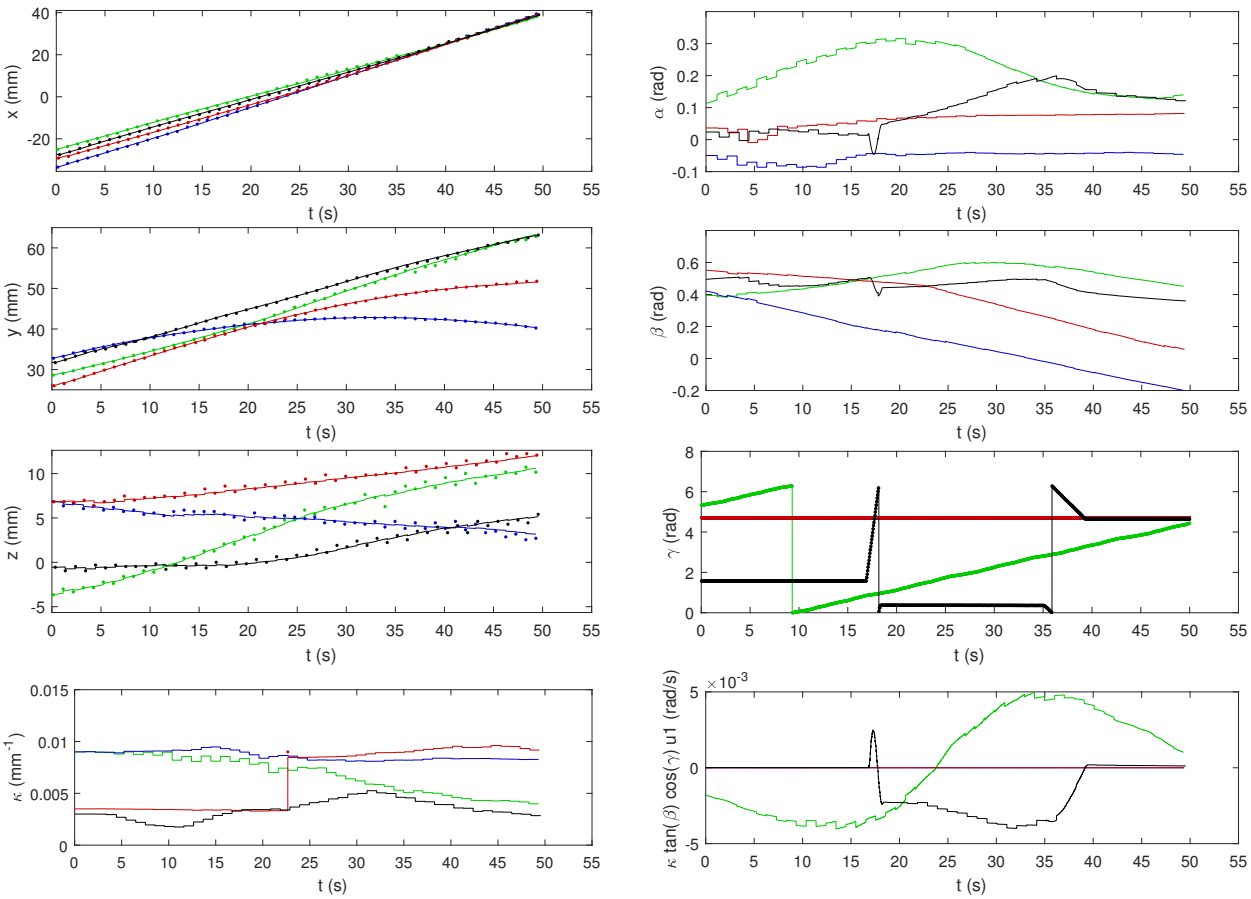

(a) Evolution of the needle tip state. Measured (dots) and estimated (curves)

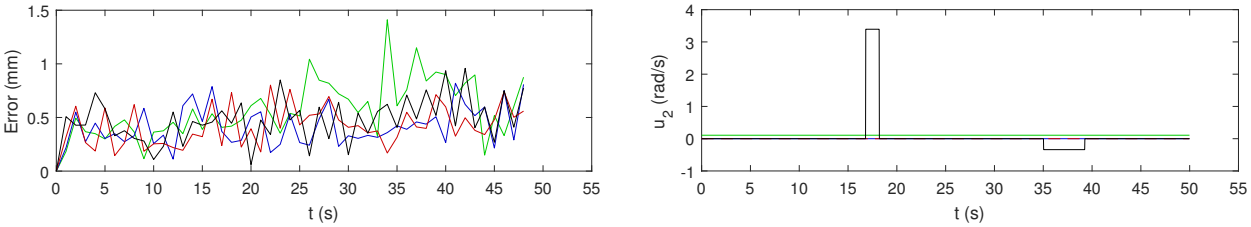

(b) Corresponding instantaneous Cartesian estimation error and rotation input u_2.

Figure 11: Estimation of the needle tip state for four independent 3D insertions at the insertion speed $u_1 = 1.5\ mm.s^{-1}$. 24 G Nitinol needle inserted in phantoms: 5% Agar phantom (blue, green), 1% Agar phantom (black) or heterogeneous 1% and 5% Agar phantom (red). The error is computed as the difference between the estimation and the measurements.

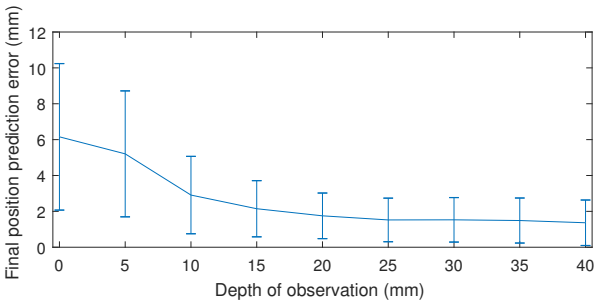

Figure 12: Mean prediction error of the final tip position (± std) as a function of the observed depth of insertion.

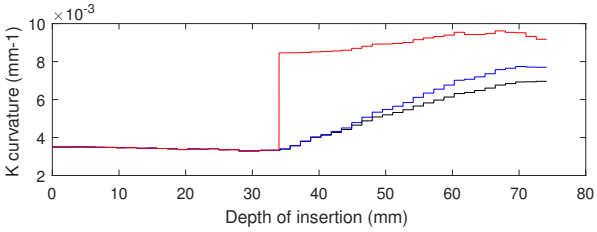

Figure 13: Evolution of the estimated radius of curvature. Without matrix reset (black). With a simple matrix reset (blue). With matrix reset and elastography measurements (red).

estimated in real time by a multi-rate unscented Kalman filter based on a modified unicycle kinematic model of the needle. Because the probe used in this study is not compatible with shear wave elastography imaging, the elastography measurements presented here are pre-operative. However, the estimator is compatible with intra-operative asynchronous elastography measurements that will be implemented in future research.

The average precision of this method is equal to 0.6±0.3 mm for instantaneous tip position estimation error. The final tip position is estimated with an error equal to 1.7±1.2 mm after observing the first 2 cm of the insertion. The precision of the instantaneous tip position estimation is on par with the works described in [8] and is more satisfactory than the results on 3D US imaging presented in [15]. The final deflection prediction is satisfactory and fully characterised. Its precision is seemingly better that the one presented in [21] although with different experimental setups. All the errors computed in the experimental section are obtained by comparison to manual segmentation since the ground truth is not available. The true precision of the system might be higher than what is presented.

The experimental validation done through 51 insertions with different needles in various media has allowed to characterise the uncertainties of the estimation and validate the robustness of the presented solution.

The proposed filtering improves targeting. Indeed, knowing both the future needle deflection and the precision of the prediction, adapted control laws can be designed. These control laws could use the information on the uncertainties to propose a robust steering. Path planning could also benefit from additional information on tissue elasticity.

Future research will focus on the integration of the current results in a robust control law. Methods for precise segmentation of the needle tip in noisy 3D US volumes using the estimation results will also be developed.

Acknowledgements

This work was partly supported by the Investissements d'Avenir programme (Labex CAMI) under reference ANR-11-LABX-0004.

References

[1] M. Abayazid, P. Moreira, N. Shahriari, S. Patil, R. Alterovitz, and S. Misra. Ultrasound-guided three-dimensional needle steering in biological tissue with curved surfaces. Medical Engineering & Physics, 37(1):145–150, Jan. 2015.

[2] M. Abayazid, R. J. Roesthuis, R. Reilink, and S. Misra. Integrating Deflection Models and Image Feedback for Real-Time Flexible Needle Steering. IEEE Transactions on Robotics, 29(2):542–553, Apr. 2013.

[3] T. K. Adebar and A. M. Okamura. Recursive estimation of needle pose for control of 3d-ultrasound-guided robotic needle steering. In Intelligent Robots and Systems (IROS 2014), 2014 IEEE/RSJ International Conference on, pages 4303–4308. IEEE, 2014.

[4] L. Armesto, S. Chroust, M. Vincze, and J. Tornero. Multi-rate fusion with vision and inertial sensors. In Robotics and Automation, 2004. Proceedings. ICRA'04. 2004 IEEE International Conference on, volume 1, pages 193–199. IEEE, 2004.

[5] J. Bercoff, M. Tanter, and M. Fink. Supersonic shear imaging: a new technique for soft tissue elasticity mapping. IEEE transactions on ultrasonics, ferroelectrics, and frequency control, 51(4):396–409, 2004.

[6] J. Carriere, C. Rossa, R. Sloboda, N. Usmani, and M. Tavakoli. Real-time needle shape prediction in soft-tissue based on image segmentation and particle filtering. In Advanced Intelligent Mechatronics (AIM), 2016 IEEE International Conference on, pages 1204–1209. IEEE, 2016.

[7] P. Chatelain, A. Krupa, and N. Navab. 3d ultrasound-guided robotic steering of a flexible needle via visual servoing. In Robotics and Automation (ICRA), 2015 IEEE International Conference on, pages 2250–2255. IEEE, 2015.

[8] J. Chevrie, A. Krupa, and M. Babel. Online prediction of needle shape deformation in moving soft tissues from visual feedback. In Intelligent Robots and Systems (IROS), 2016 IEEE/RSJ International Conference on, pages 2375–2380. IEEE, 2016.

[9] B. Fallahi, C. Rossa, R. S. Sloboda, N. Usmani, and M. Tavakoli. Sliding-based image-guided 3d needle steering in soft tissue. Control Engineering Practice, 63:34–43, June 2017.

[10] C. Fouard, A. Deram, Y. Keraval, and E. Promayon. CamiTK: A Modular Framework Integrating Visualization, Image Processing and Biomechanical Modeling. In Y. Payan, editor, Soft Tissue Biomechanical Modeling for Computer Assisted Surgery, volume 11, pages 323–354. Springer Berlin Heidelberg, Berlin, Heidelberg, 2012.

[11] J. Huang, J. K. Triedman, N. V. Vasilyev, Y. Suematsu, R. O. Cleveland, and P. E. Dupont. Imaging Artifacts of Medical Instruments in Ultrasound-Guided Interventions. Journal of Ultrasound in Medicine, 26(10):1303–1322, 2007.

[12] N. Hungr, M. Baumann, J.-A. Long, and J. Troccaz. A 3-D ultrasound robotic prostate brachytherapy system with prostate motion tracking. IEEE Transactions on Robotics, 28(6):1382–1397, 2012.

[13] M. Khadem, C. Rossa, R. S. Sloboda, N. Usmani, and M. Tavakoli. Ultrasound-Guided Model Predictive Control of Needle Steering in Biological Tissue. Journal of Medical Robotics Research, 01(01):1640007, Mar. 2016.

[14] P. Mignon, P. Poignet, and J. Troccaz. Using rotation for steerable needle detection in 3d color-Doppler ultrasound images. In Engineering in Medicine and Biology Society (EMBC), 2015 37th Annual International Conference of the IEEE, pages 1544–1547. IEEE, 2015.

[15] P. Mignon, P. Poignet, and J. Troccaz. Beveled-tip needle-steering using 3d ultrasound, mechanical-based Kalman filter and curvilinear ROI prediction. In Control, Automation, Robotics and Vision (ICARCV), 2016 14th International Conference on, pages 1–6. IEEE, 2016.

[16] P. Mignon, P. Poignet, and J. Troccaz. Automatic Robotic Steering of Flexible Needles from 3d Ultrasound Images in Phantoms and Ex Vivo Biological Tissue. Annals of Biomedical Engineering, May 2018.

[17] P. Moreira and S. Misra. Biomechanics-based curvature estimation for ultrasound-guided flexible needle steering in biological tissues. Annals of biomedical engineering, 43(8):1716–1726, 2015.

[18] S. Patil, J. Burgner, R. J. Webster, and R. Alterovitz. Needle Steering in 3-D Via Rapid Replanning. IEEE Transactions on Robotics, 30(4):853–864, Aug. 2014.

[19] G. Reusz, P. Sarkany, J. Gal, and A. Csomos. Needle-related ultrasound artifacts and their importance in anaesthetic practice. British Journal of Anaesthesia, 112(5):794–802, May 2014.

[20] C. Rossa, T. Lehmann, R. Sloboda, N. Usmani, and M. Tavakoli. A data-driven soft sensor for needle deflection in heterogeneous tissue using just-in-time modelling. Medical & Biological Engineering & Computing, 55(8):1401–1414, Aug. 2017.

[21] M. Waine, C. Rossa, R. Sloboda, N. Usmani, and M. Tavakoli. Needle Tracking and Deflection Prediction for Robot-Assisted Needle Insertion Using 2d Ultrasound Images. Journal of Medical Robotics Research, 01(01):1640001, Mar. 2016.

[22] E. A. Wan and R. Van Der Merwe. The unscented Kalman filter for nonlinear estimation. In Adaptive Systems for Signal Processing, Communications, and Control Symposium 2000. AS-SPCC. The IEEE 2000, pages 153–158. Ieee, 2000.

[23] R. J. Webster, J. S. Kim, N. J. Cowan, G. S. Chirikjian, and A. M. Okamura. Nonholonomic Modeling of Needle Steering. The International Journal of Robotics Research, 25(5-6):509–525, May 2006.

Appendix A. State of the art

Author	Chevrie	Moreira	Carriere	Waine	Adebar	Chatelain	Mignon	This paper
Article	[8]	[17]	[6]	[21]	[3]	[7]	[15]	
Year	2016	2015	2016	2016	2014	2015	2016	2018
Sensor	CCD cameras	US 2,5D B-Mode	US 2,5D B-Mode	US 2,5D B-Mode	US 3D Doppler	US 3D B-Mode	US 3D B-Mode	US 3D B-Mode
Sensor frequency	30Hz & 1Hz	25Hz	20Hz	20Hz	0,3Hz	3,3Hz	1Hz	1Hz
2D/3D steering	3D	3D	2D	2D	3D	3D	3D	3D
Model	Beam	Unicycle	Bicycle	Beam	Unicycle	Polynomial	Virtual Springs	Bicycle
Observer	UKF	KF	PF	Extr.	UKF	PF	KF	MR-UKF
Online curvature estimation	N/A	X	X	N/A		N/A	N/A	X
Variable tissue stiffness		X						X
Tissue deformation	X							
Lenth of insertion (mm)	100	80	120	140	100	80	80	80
Instantaneous error (mm)	0,7±0,5 @1Hz	<0,74	N/A	N/A	N/A	N/A	1,06±0,15	0,6±0,3
Prediction error* (mm)	N/A	N/A	8	3,5	N/A	N/A	N/A	1,7±1,2
Number of insertions	3	15	6	48	6	1	26	51
Needles	19G, 22G, 25G S-BT	24G N-BT	18G S-BT	18G S-BT	23G S-BT	22G S-BT	24G N-PC	24G S-PC, S-BT, N-BT
Validation media	Phantom	Ex-Vivo	Clinical data	Ex-Vivo	Ex-Vivo	Phantom	Phantom	Ex-Vivo

Table A.3: Sum-up table of observers in needle steering. KF : Kalman filter, UKF : unscented Kalman Filter, MR-UKF : multi-rate unscented Kalman filter, PF : particle filter, Extr. : extrapolation, N/A : not available or not applicable, S-BT : Steel bevel-tip needle, N-BT : Nitinol bevel-tip needle, S-PC : Steel pre-curved needle, N-PC : Nitinol pre-curved needle.
*Prediction error calculated after observing 25% of the insertion length.

Appendix B. Equations of the proposed multi-rate unscented Kalman filter

Compute weight

$$\begin{aligned} W_{0_m} &= \lambda/(n+\lambda) \\ W_{0_c} &= \lambda/(n+\lambda) + (1-\alpha^2+\beta) \\ W_{i_m} = W_{i_c} &= 1/(2(n+\lambda)) \end{aligned}$$

$\lambda = \alpha^2(n+\kappa) - n.$ $\quad i = 1, .., 2n.$
α, β and κ are scaling parameters introduced in 3.2.

Reset matrices

$$\begin{aligned} \mathbf{P}_{k-1|k-1} &= \mathbf{P}'_k \\ \mathbf{R}_k &= \mathbf{R}'_k \end{aligned}$$

$\mathbf{P}'_k$ and $\mathbf{R}'_k$ being calculated as detailed in 2.3.

Calculate sigma points

$$\begin{aligned} \boldsymbol{\mathcal{X}}_{0,k-1|k-1} &= \hat{\mathbf{x}}_{k-1|k-1} \\ \boldsymbol{\mathcal{X}}_{i,k-1|k-1} &= \hat{\mathbf{x}}_{k-1|k-1} + \left(\sqrt{(n+\lambda)\mathbf{P}_{k-1|k-1}}\right)_i \\ \boldsymbol{\mathcal{X}}_{i+n,k-1|k-1} &= \hat{\mathbf{x}}_{k-1|k-1} - \left(\sqrt{(n+\lambda)\mathbf{P}_{k-1|k-1}}\right)_i \end{aligned}$$

$(\mathbf{M})_i$ is the ith column of the matrix $\mathbf{M}$.

Predict sigma points

$$\boldsymbol{\mathcal{X}}_{i,k|k-1} = \mathbf{f}(\boldsymbol{\mathcal{X}}_{i,k-1|k-1}, u)$$

With $\mathbf{f}(\mathbf{x}, \mathbf{u})$ detailed in eq.(1).

Predict

$$\begin{aligned} \hat{\mathbf{x}}_{k|k-1} &= \sum_{i=0}^{2n} W_{i_m} \boldsymbol{\mathcal{X}}_{i,k|k-1} \\ \mathbf{P}_{k|k-1} &= \Big(\sum_{i=0}^{2n} W_{i_c} \left[\boldsymbol{\mathcal{X}}_{i,k|k-1} - \hat{\mathbf{x}}_{k|k-1}\right] \\ &\quad \left[\boldsymbol{\mathcal{X}}_{i,k|k-1} - \hat{\mathbf{x}}_{k|k-1}\right]^\top \Big) + \mathbf{Q} \end{aligned}$$

Update sigma points

$$\boldsymbol{\mathcal{Y}}_{\Delta\, i,k|k-1} = \mathbf{h}_\Delta\left(\boldsymbol{\mathcal{X}}_{i,k|k-1}\right)$$

With $\mathbf{h}(\mathbf{x})$ detailed in eq.(2).
Δ indicates the matrices that change size accordingly to the measurements.
Only the sigma points of the available measurements are calculated and propagated.

Update

$$\begin{aligned} \hat{\mathbf{y}}_{\Delta\, k|k-1} &= \sum_{i=0}^{2n} W_{i_m} \boldsymbol{\mathcal{Y}}_{\Delta\, i,k|k-1} \\ \mathbf{P}_{\Delta\, yy,k|k-1} &= \Big(\sum_{i=0}^{2n} W_{i_c} \left[\boldsymbol{\mathcal{Y}}_{\Delta\, i,k|k-1} - \hat{\mathbf{y}}_{\Delta\, k|k-1}\right] \\ &\quad \left[\boldsymbol{\mathcal{Y}}_{\Delta\, i,k|k-1} - \hat{\mathbf{y}}_{\Delta\, k|k-1}\right]^\top \Big) + \mathbf{R}_{\Delta\, k} \\ \mathbf{P}_{\Delta\, xy,k|k-1} &= \sum_{i=0}^{2n} W_{i_c} \left[\boldsymbol{\mathcal{X}}_i(k|k-1) - \hat{\mathbf{x}}(k|k-1)\right] \\ &\quad \left[\boldsymbol{\mathcal{Y}}_{\Delta\, i}(k|k-1) - \hat{\mathbf{y}}_\Delta(k|k-1)\right]^\top \\ \mathbf{K}_{\Delta\, k} &= \mathbf{P}_{\Delta\, xy,k|k-1} \mathbf{P}^{-1}_{\Delta\, yy,k|k-1} \\ \mathbf{P}_{k|k} &= \mathbf{P}_{k|k-1} - \mathbf{K}_{\Delta\, k} \mathbf{P}_{\Delta\, yy,k|k-1} \mathbf{K}^\top_{\Delta\, k} \\ \hat{\mathbf{x}}_{k|k} &= \hat{\mathbf{x}}_{k|k-1} + \mathbf{K}_{\Delta\, k}(\mathbf{y}_{\Delta\, k} - \hat{\mathbf{y}}_{\Delta\, k|k-1}) \end{aligned}$$

Constraint curvature

$$\hat{\mathbf{x}}_{k|k}(7) = \hat{\kappa}_{k|k} = \begin{cases} \hat{\kappa}_{k|k} & \text{if } 0 \le \hat{\kappa}_{k|k} \le \kappa_{max} \\ \hat{\kappa}_{k-1|k-1} & \text{else} \end{cases}$$

nb: $\hat{\mathbf{x}}$ is the state estimate. $\mathbf{y}$ is the measurement vector.